PNAS RESEARCH ARTICLE | PHYSICS OPEN ACCESS

Observation of emergent scaling of spin–charge correlations at the onset of the pseudogap

Thomas Chalopin[a,b,c,1], Petar Bojović[a,b], Si Wang[a,b], Titus Franz[a,b], Aritra Sinha[d], Zhenjiu Wang[e,f,g], Dominik Bourgund[a,b], Johannes Obermeyer[a,b], Fabian Grusdt[b,e,f], Annabelle Bohrdt[b,h], Lode Pollet[b,e,f], Alexander Wietek[d], Antoine Georges[i,j,k,l], Timon Hilker[a,b,m], and Immanuel Bloch[a,b,e,g,1]

Affiliations are included on p. 7.

Contributed by Immanuel Bloch; received September 14, 2025; accepted December 23, 2025; reviewed by Andrey Chubukov and Tilman Esslinger

In strongly correlated materials, interacting electrons are entangled and form collective quantum states, resulting in rich low-temperature phase diagrams. Notable examples include cuprate superconductors, in which superconductivity emerges at low doping out of an unusual "pseudogap" metallic state above the critical temperature. The Fermi–Hubbard model, describing a wide range of phenomena associated with strong electron correlations, still offers major computational challenges despite its simple formulation. In this context, ultracold atoms quantum simulators have provided invaluable insights into the microscopic nature of correlated quantum states. Here, we use a quantum gas microscope Fermi–Hubbard simulator to explore a wide range of dopings and temperatures in a regime where a pseudogap is known to develop. By measuring multipoint correlation functions up to fifth order, we uncover a universal scaling behavior in magnetic and higher-order spin–charge correlations characterized by a doping-dependent temperature scale. Accurate comparisons with determinant Quantum Monte Carlo and Minimally Entangled Typical Thermal States simulations confirm that this temperature scale is comparable to the pseudogap temperature T^*. Our quantitative findings reveal a qualitative behavior of magnetic properties and spin–charge correlations in an emergent pseudogap and pave the way toward the exploration of charge pairing and collective phenomena expected at lower temperatures.

quantum simulation | Fermi-Hubbard | strongly correlated electrons | pseudogap | ultracold atoms

Significance

Understanding strongly correlated fermions constitutes a major challenge of modern physics. Here, we take a significant step in this direction, by the finding of a universal scaling of spin and charge correlations upon entering the pseudogap phase in the paradigmatic Hubbard model, using our ultracold atom quantum simulator. This leads to a quantitative description of how doping suppresses the spin stiffness, concurrent with the emergence of dominant higher-order correlations that we observe in the system. Our characterization of the magnetic properties of the pseudogap in the paradigmatic Hubbard model paves the way for future studies of further collective phases of matter that the pseudogap is believed to give way to at even lower temperatures.

The Fermi–Hubbard model (FHM) is a minimal but at the same time paradigmatic model for describing interacting fermions on a lattice (1). The conjectured phase diagram of the two-dimensional (2D) FHM, as a function of temperature and doping (or excess charge carrier density), is depicted in Fig. 1*C*, as inferred in part from recent computational studies (2). It features an insulating ground state at half-filling with antiferromagnetic (AFM) long-range order, which becomes stripe (magnetic and charge) ordered when doped. Superconducting long-range order has also been reported upon doping, with the delicate interplay between superconductivity and stripe ordering depending on details of the model (3, 4). The two-dimensional FHM is widely regarded as capturing essential qualitative features of strongly correlated materials (5, 6) such as the cuprate compounds (7, 8), which are notably known for exhibiting high-T_c superconductivity.

At higher temperatures, the metallic phase of the FHM features a "pseudogap" below a characteristic temperature T^* (2, 9–12), i.e., a partial depletion of the density of states at the Fermi level (13–15). This pseudogap is analogous to the one found in the underdoped region of cuprates, especially when magnetic correlations are predominant, and was first identified in such materials through magnetic susceptibility measurements (16, 17). The physical origin of the pseudogap in cuprates has long been debated. Some explanations emphasize its connection to magnetic correlations (15, 18–20) and relation to the stripe phase (21, 22). Possible magnetic or charge ordering instabilities of the pseudogap state have also been widely discussed (23–25). It is sometimes also considered as a precursor of the superconducting state (14), similar to the phenomenology found in unitary Fermi gases, where a pseudogap develops above the critical temperature for superfluidity (26–28).

Over the past few years, tremendous progress has been made both from an experimental and theoretical perspective toward a better understanding of the microscopic nature of strongly correlated phases emerging in the FHM and its derivatives. Quantum gas microscopes, in particular, have provided valuable insights into the formation of spin-ordered phases (29–31), the interplay between spin and charge degrees of freedom

Author contributions: T.C. led the project; T.C. and P.B. contributed significantly to data collection; T.C. analyzed the data; A.S. and A.W. performed the METTS simulations and the associated data analysis; Z.W. and L.P. performed the dQMC calculations; F.G. and A.B. performed the geometric string calculations; T.C. and A.G. wrote the manuscript; and T.H. and I.B. supervised the study. All authors interpreted data and contributed to the final manuscript.

Reviewers: A.C., University of Minnesota; and T.E., ETH Zurich.

The authors declare no competing interest.

[1]To whom correspondence may be addressed. Email: thomas.chalopin@institutoptique.fr or immanuel.bloch@mpq.mpg.de.

This article contains supporting information online at https://www.pnas.org/lookup/suppl/doi:10.1073/pnas.2525539123/-/DCSupplemental.

Published January 23, 2026.

(32–39), the emergence of charge-ordered states (40, 41), and transport properties (42–44). A systematic exploration of the 2D FHM, varying both temperature and doping, is however still lacking. Numerical methods, on the other hand, are increasingly arriving at a consensus regarding the physics of the 2D FHM in certain regimes (2, 45, 46). Stripe order has been confirmed by numerous methods as the ground state at finite doping and intermediate coupling strengths (45, 47–50), the pseudogap regime has been tied to the onset of antiferromagnetic correlations (12, 18, 19, 46, 51, 52) and charge clustering (53), and superconductivity has been found to be strongly enhanced upon adding next-nearest neighbor hopping (4, 54–57).

In this work, we perform a systematic exploration of the 2D FHM over a dense grid of dopings and temperatures (Fig. 1*C*) using a quantum gas microscope Fermi–Hubbard simulator (Fig. 1*A*) and uncover a universal scaling in spin and spin–charge correlations. We use these correlation functions to provide a microscopic description of the underlying strongly correlated states, especially in a regime where the presence of a pseudogap is well established (12, 18, 19, 51, 52). We compare our measurements to different numerical methods (Fig. 1*D*), including determinant Quantum Monte Carlo (dQMC) (58, 59), Minimally Entangled Typical Thermal States (METTS) (51, 60–62)—a method based on matrix-product states—and an effective model based on chargon-spinon geometric strings (63).

1. Experimental Protocol

Our experiment consists in loading a spin-balanced ultracold gas of ^{6}Li atoms in a 2D optical lattice (64, 65), which naturally implements the FHM with Hamiltonian

$$\hat{H} = -t \sum_{\langle \boldsymbol{i},\boldsymbol{j}\rangle,\sigma} \hat{c}^{\dagger}_{\boldsymbol{i},\sigma}\hat{c}_{\boldsymbol{j},\sigma} + \text{h.c.} + U\sum_{\boldsymbol{i}} \hat{n}_{\boldsymbol{i},\uparrow}\hat{n}_{\boldsymbol{i},\downarrow}. \qquad [1]$$

Here, t and U denote the tunneling and (on-site) interaction energies, $\sigma = \uparrow, \downarrow$ is the spin, $\hat{c}_{\boldsymbol{i},\sigma}$ ($\hat{c}^{\dagger}_{\boldsymbol{i},\sigma}$) is the fermionic annihilation (creation) operator for spin σ on site $\boldsymbol{i}$, $\hat{n}_{\boldsymbol{i},\sigma} = \hat{c}^{\dagger}_{\boldsymbol{i},\sigma}\hat{c}_{\boldsymbol{i},\sigma}$, and $\langle \boldsymbol{i},\boldsymbol{j}\rangle$ designate nearest-neighbor (NN) lattice sites. The optical potential is engineered using a Digital Micromirror Device (DMD) such as to have a homogeneous system of $|\Omega| = 145$ lattice sites surrounded by a low-density reservoir (Fig. 1*B*), whose chemical potential is adjusted to control the central particle density $\langle \hat{n}_{\boldsymbol{i}}\rangle$ (*SI Appendix*). The temperature of the system can be tuned by holding the atoms in the lattice for a variable time, naturally causing heating (30). Throughout this work, tunnelling and interaction energies are set to $t/h = 300(25)$Hz and $U/h = 1.95(5)$ kHz, such that $U/t = 6.5(5)$. This choice is motivated by recent theoretical work showing the maximum extent of the pseudogap phase as a function of doping at temperature ranges relevant to this work (12, 19). Detection is performed using a quantum gas microscope, allowing for spin and charge resolution (Fig. 1*A*), as described in our recent work (41, 66).

We collected 36,485 snapshots at various dopings and heating durations and binned them accordingly. In particular, we evaluate for each bin the system-averaged, normalized, and connected spin correlation function

$$C^{(2)}_{\text{ss}}(\boldsymbol{d}) = \frac{4}{\mathcal{N}_{\boldsymbol{d}}}\sum_{\boldsymbol{i}\in\Omega}\langle \hat{S}^z_{\boldsymbol{i}}\hat{S}^z_{\boldsymbol{i}+\boldsymbol{d}}\rangle_{\text{c}}, \qquad [2]$$

and bin together datasets with similar density and NN correlations $C^{(2)}_{\text{ss}}(|\boldsymbol{d}| = 1)$, which we use as a proxy for the temperature. In the above expression, $\mathcal{N}_{\boldsymbol{d}}$ is a normalization constant that counts the number of pairs of lattice sites separated by $\boldsymbol{d}$, $\hat{S}^z_{\boldsymbol{i}} = (\hat{n}_{\boldsymbol{i},\uparrow} - \hat{n}_{\boldsymbol{i},\downarrow})/2$ is the z-component of the spin operator on lattice site $\boldsymbol{i}$, and $\langle\cdot\rangle_{\text{c}}$ designates connected correlations. We refer the reader to *SI Appendix* for additional information regarding the exact definition of connected correlation functions, our binning procedure, and the effect of finite detection fidelity on our observables.

The above-described procedure results in about 120 datasets of 5%-wide doping bins, with $-30\% \le \delta = \langle \hat{n}_{\boldsymbol{i}}\rangle - 1 \le 30\%$. For each dataset, we compare the radially averaged spin correlations $C^{(2)}_{\text{ss}}(|\boldsymbol{d}|)$ to dQMC simulations performed at various dopings and temperatures (Fig. 2*A* and *SI Appendix*). We observe excellent agreement between the experimental and numerical data with temperature as the only adjustable parameter. This procedure thus allows the assignment of a temperature to each dataset, ranging from $T/t \approx 0.2$ to $T/t \approx 1$ (the Boltzmann constant is set to $k_{\text{B}} = 1$). The results are furthermore compared to METTS (Fig. 2*B*), which also shows an excellent agreement with both the experimental and dQMC data. The range of doping and temperature explored in this work is indicated by the hatched region in Fig. 1*C*.

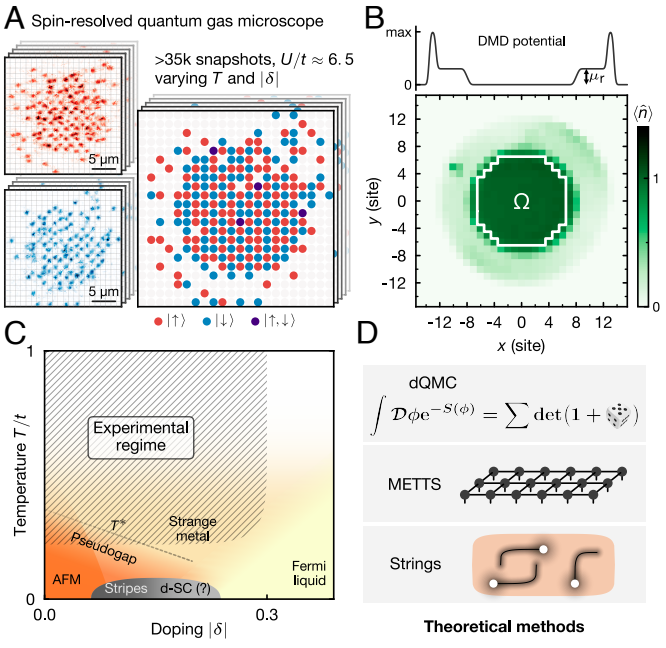

Fig. 1. Quantum simulation of the FHM. (*A*) Examples of experimental snapshots using a quantum gas microscope with spin and charge resolution. (*B*) Averaged atomic density, depicting the central region (Ω) over which the analysis is carried out, and the surrounding reservoir with chemical potential μ_r experimentally adjusted using a DMD (*SI Appendix*). (*C*) Conjectured phase diagram of the FHM. The hatched region approximately depicts the regime accessed by our experimental apparatus. AFM: region with sizeable antiferromagnetic correlations. d-SC: conjectured superconducting phase. (*D*) Theoretical methods employed in this work: dQMC, METTS, and geometric strings (see text).

2. Spin Correlations

In the thermodynamic limit, the Mermin–Wagner theorem prevents true long-range order at any finite temperature in the 2D FHM (67). Nevertheless, close to half-filling, AFM correlations

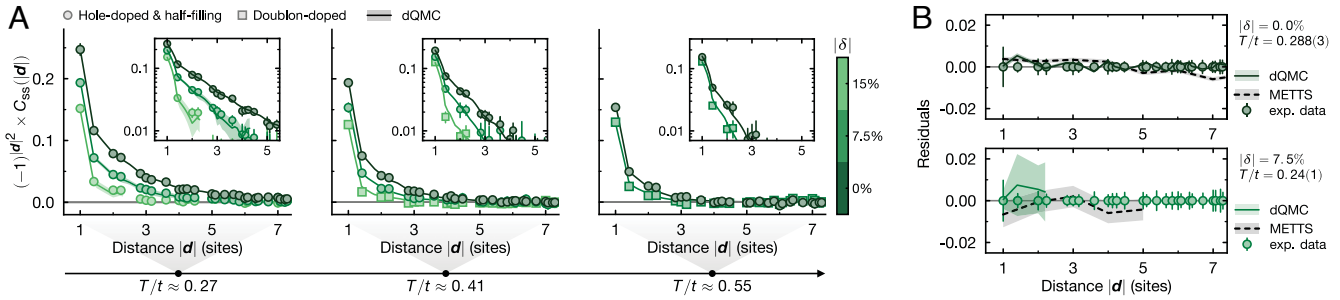

Fig. 2. Thermometry. (*A*) The temperature of the experimental datasets is extracted by finding the best fit between dQMC numerical calculations (solid lines) and the measured spin correlations $C_{ss}^{(2)}(|\boldsymbol{d}|)$ (data points), with the temperature being the only fitting parameter. Experimental errorbars in this figure and in all figures correspond to the 68% CI of a bootstrap analysis (*SI Appendix*). (*B*) Residuals between dQMC and experiment (solid line) and comparison to METTS (dashed line), taking the experimental data points as a reference, for half-filling (*Top*) and at $|\delta| = 7.5\%$ doping (*Bottom*). Here, METTS is computed on a 32×4 cylinder, and dQMC on a square with periodic boundary conditions of size 16×16 (half-filling) or 10×10 (finite doping). Numerical errorbars (*SI Appendix*) in this figure and in all figures are indicated by shaded regions.

become more and more prominent as the temperature decreases. Here, we measure spin correlations which are significantly nonzero up to more than seven sites, a distance comparable to the radius of our system. In order to characterize the strength and range of spin correlations, we compute the spin structure factor $\mathcal{S}(\boldsymbol{q})$, defined as the Fourier transform of the spin correlations

$$\mathcal{S}(\boldsymbol{q}) = \sum_{\boldsymbol{d}\in\Phi} e^{i\boldsymbol{q}\boldsymbol{d}} C_{ss}^{(2)}(\boldsymbol{d}), \qquad [3]$$

where Φ, represented by the gray square in Fig. 3*C*, corresponds to the region $\max(d_x, d_y) \leq 7$ sites. We show in Fig. 3*B* the spin structure factor computed from the data in Fig. 3*A*, depicting a strong peak centered at $\boldsymbol{q}_{\mathrm{AFM}} = (\pi, \pi)$ as a manifestation of sizeable and extended AFM correlations. We emphasize that, given the experimental temperature and resolution achieved here (Fig. 1*C*), we do not detect a shift of the ordering vector away from (π, π) expected at low temperatures (49, 68) as a possible precursor to stripe ordering (50, 51). Note that the structure factor we consider here is associated with the equal-time correlation function, and not the usual static (zero-frequency) one (21).

We extract the peak structure factor $\mathcal{S}_{\mathrm{AFM}} \equiv \mathcal{S}(\boldsymbol{q} = \boldsymbol{q}_{\mathrm{AFM}})$ for each dataset, and give the results in Fig. 3*C*. There, each point corresponds to a single dataset, and a Delaunay triangulation is performed to pave the (δ, T) space: the color of each triangle is given by the average value of $\mathcal{S}_{\mathrm{AFM}}$ over all three of its vertices. As expected from the particle–hole symmetry of the FHM on a bipartite lattice* (69), the peak structure factor appears symmetric with respect to half-filling, i.e., hole doping ($\delta < 0$) and doublon doping ($\delta > 0$) have identical effects on the spin correlations. We clearly observe an increase of $\mathcal{S}_{\mathrm{AFM}}$ as dopings get closer to half-filling and the temperature is reduced.

The temperature dependence of the measured peak structure factor is found to be well described by an exponential form:

$$\mathcal{S}_{\mathrm{AFM}}(\delta, T) \sim e^{2\Theta(\delta)/T}, \qquad [4]$$

with $\Theta(\delta)$ a doping-dependent temperature scale. This form is motivated by the relation $\mathcal{S}_{\mathrm{AFM}} \sim \xi^2$ between the peak structure factor and the spin correlation length ξ, as given by the Ornstein-Zernike form (46). The exponential dependence for ξ is indeed expected when the ground-state of a 2D quantum system displays long-range spin ordering, in which case, the scale Θ identifies with the spin stiffness $2\pi\rho_s$ (70). Given the range of temperatures accessible to our experiments (Fig. 1*C*), we cannot ascertain that the exponential fit persists down to low-T and thus whether the ground-state displays long-range spin order; $\Theta(\delta)$ should be viewed as an empirically defined spin stiffness whose doping dependence is determined from experiments. In essence, expression [4] describes how a reduction in AFM order through doping can be compensated for by further cooling the system.

To determine the doping dependence of Θ, we introduce a second-order expansion *Ansatz* of the form $\Theta(\delta) = \Theta^{(0)} + \Theta^{(1)}|\delta| + \Theta^{(2)}|\delta|^2$, where the $\Theta^{(i)}$ coefficients are fit parameters. The coefficient $\Theta^{(0)}$ is determined by fitting the half-filled data, to find $\Theta^{(0)}/t = 0.32(4)$. The other two coefficients are determined through an optimization procedure that aligns the $\mathcal{S}_{\mathrm{AFM}}(T, \delta)$ curves to a universal form $\mathcal{S}_{\mathrm{AFM}}[\Theta(\delta)/T]$, as described by Eq. **4**. The procedure, described in more detail in *SI Appendix*, yields $\Theta^{(1)}/t = -1.6(4)$ and $\Theta^{(2)}/t = 2(2)$. The result of the optimization is shown as the black line in Fig. 3 *C* and *F*.

Remarkably, we find an excellent collapse of the magnetic peak structure factor $\mathcal{S}_{\mathrm{AFM}}[\Theta(\delta)/T]$ following the above procedure for all doping and temperatures explored here (see Fig. 3*D* and its *Lower Inset*). The collapse only depends on the absolute value of doping and holds for both hole- and particle-doped systems (disk and square symbols, respectively). In contrast, the unscaled raw data exhibita distinctly doping-dependent behavior (see Fig. 3 *D*, *Top Inset*).

We compare the extracted $\Theta(\delta)$ to the expected temperature T^* that marks the crossover to the pseudogap regime in the FHM. Although the opening of a pseudogap is nowadays commonly identified through ARPES measurements (71), the pseudogap in cuprates was originally identified through the temperature dependence of the magnetic susceptibility χ_m(16, 17). In the Hubbard model, numerical studies have revealed that the uniform susceptibility displays a maximum at a temperature T^* which can serve as a definition of the pseudogap onset temperature (51, 72). Here, the value of T^* is obtained from the maximum of χ_m in METTS simulations, as shown in Fig. 3*E*, and compared to $\Theta(\delta)$ in Fig. 3*F*. T^* (from METTS) and Θ (from the experimental data) are relatively close in amplitude and are decreasing functions of δ. The extracted value of Θ is comparable but slightly smaller than T^*, suggesting that the universal scaling associated with Θ that we observe experimentally

*The particle–hole symmetry here means that hole- and doublon-doped exhibit the exact same physical properties. In practice, we found experimentally that we can reach lower temperatures in hole-doped systems. We exploit this symmetry in evaluating higher-order correlators (Sections 3 and 4) by mixing both hole-doped and doublon-doped sectors, thus improving statistics (*SI Appendix*).

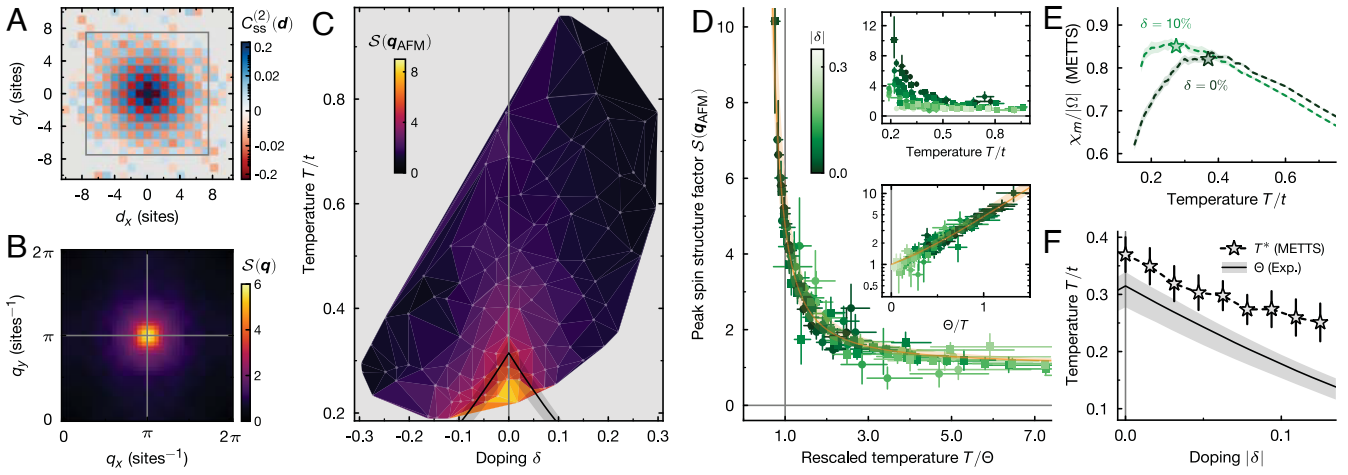

Fig. 3. Magnetic correlations in the pseudogap. (*A*) Spin correlation map at $T/t = 0.25(1)$ and $\delta \approx -2.5\%$. (*B*) Symmetrized spin structure factor $\mathcal{S}(\boldsymbol{q})$ evaluated from a subregion of the spin correlation map (gray square in *A*). (*C*) Peak structure factor $\mathcal{S}_{\mathrm{AFM}}$ as a function of doping δ and temperature T/t. Each vertex is a data point, and each triangle is colored according to the average of its vertices. The black line corresponds to the experimentally extracted doping-dependent energy scale $\Theta(\delta)$ (see panel *D*). (*D*) Peak structure factor as a function of the rescaled temperature T/Θ (see text), with the orange line showing the exponential dependence of Eq. **4**. Both *Insets* show the same data, without rescaling (*Top*) and in semi-log-scale (*Bottom*). (*E*) Magnetic susceptibility extracted from METTS numerical simulations, for $\delta = 0$ and $\delta = 0.1$. The maximum of susceptibility (stars) occurs at $T = T^*$, is doping dependent, and marks the crossover to the pseudogap phase. (*F*) Comparison between $\Theta(\delta)$, extracted from the $\mathcal{S}_{\mathrm{AFM}}$ collapse (panel *D*) and T^* extracted from METTS.

is linked to the opening of the pseudogap in the system. We stress here that we are not aware of a previous study that attempts to relate Θ—a doping-dependent spin stiffness—to T^*. Nevertheless, Monte-Carlo simulations on the Heisenberg model have shown that the temperature T^* marking the maximum of spin susceptibility coincides with the spin stiffness $2\pi\rho_s$ (73). Although no formal relation can be established, our results suggest that these quantities reflect the same underlying phenomenology.

The connection between the pseudogap and AFM spin-correlations is well established theoretically in the weak-coupling regime when the correlation length reaches large values. In this regime, the Vilk-Tremblay spin fluctuation theory states that a pseudogap opens when ξ exceeds the de Broglie thermal wavelength $\sim v_{\mathrm{F}}/\pi T$, where v_{F} is a typical Fermi velocity [(74), see also refs. 46, 75, and 76]. We note that this criterion is not satisfied here, with $1 \lesssim \xi \approx \sqrt{\mathcal{S}_{\mathrm{AFM}}} \lesssim 3$, while $2 \lesssim v_{\mathrm{F}}/\pi T \lesssim 4$. Nonetheless, we find that the universal scaling $T^* \sim \Theta \sim T \log \xi$ relating the pseudogap temperature to the correlation length at weak coupling appears to have a wider range of applicability, extending to the stronger coupling regime investigated here. Thus, our results provide evidence that the pseudogap regime in the FHM at intermediate to strong coupling is concomitant to the emergence of a strongly correlated regime marked by spin correlations of moderate spatial extension. This picture is indeed consistent with computational studies (18, 19, 51, 77), which also confirm that a pseudogap emerges in the range of parameters reached in our experiment (12).

3. Dopant-Spin–Spin Correlations

We now turn to higher-order correlations in order to explore how the interplay between dopants and spins behaves when entering the strongly correlated regime associated with $T \leq \Theta \simeq T^*$. In particular, we evaluate third-order, connected, and normalized dopant–spin–spin correlations as

$$C^{(3)}_{\mathrm{dss}}(\boldsymbol{r},\boldsymbol{d}) = \frac{4}{\mathcal{N}_{\boldsymbol{r},\boldsymbol{d}}} \sum_{\boldsymbol{i}\in\Omega} \frac{\langle \hat{d}_{\boldsymbol{i}} \hat{S}^z_{\boldsymbol{i}+\boldsymbol{r}+\boldsymbol{d}/2} \hat{S}^z_{\boldsymbol{i}+\boldsymbol{r}-\boldsymbol{d}/2} \rangle_{\mathrm{c}}}{\langle \hat{d}_{\boldsymbol{i}} \rangle}, \qquad [5]$$

where $\mathcal{N}_{\boldsymbol{r},\boldsymbol{d}}$ is a normalization constant. $C^{(3)}_{\mathrm{dss}}$ evaluates how spin correlations between two spins separated by $\boldsymbol{d}$ are affected by the presence of a dopant at distance $\boldsymbol{r}$ from the spin bond, and characterizes the spatial structure of magnetic polarons (33, 35, 38). We limit our analysis to NN ($|\boldsymbol{d}| = 1$), NNN ($|\boldsymbol{d}| = \sqrt{2}$), and second NN ($|\boldsymbol{d}| = 2$) spin bonds. For the remainder of the manuscript, we rely on the particle–hole symmetry of the Hubbard model and combine both hole- and doublon-doped sectors to improve statistics* (*SI Appendix*). Thus, in Eq. **5**, the operator $\hat{d}_{\boldsymbol{i}}$ is the dopant operator at lattice site $\boldsymbol{i}$ (*SI Appendix*). The experimental measurements of higher-order correlators are compared to calculations from METTS, dQMC and from the geometric string model. In the case of METTS and the string model, classical snapshots akin to that of the quantum gas microscope are sampled (*SI Appendix*).

In Fig. 4*A*, we present examples of symmetrized polaron correlation maps at different dopings and temperatures for NN ($|\boldsymbol{d}| = 1$) and NNN ($|\boldsymbol{d}| = \sqrt{2}$) spin bonds. Close to half-filling ($|\delta| \approx 5\%$) and at low temperatures, we observe significant nonzero correlations over a disk of radius $|\boldsymbol{r}| \approx 4$ around the dopant (gray circles in Fig. 4*A*), indicating that a single dopant affects the background AFM order over a surrounding region that spans more than 50 lattice sites. As either the doping or the temperature increases, the size of the polaron decreases.

In Fig. 4 *B*, we show the sign-corrected and distance-averaged correlations to clearly evaluate the range over which connected correlations remain nonzero for the coldest datasets ($T/t < 0.3$). We systematically observe nonzero correlations at short ranges—i.e., in the core of the magnetic polarons corresponding to the spin bonds in the direct vicinity of the dopant—for all temperature and doping values studied here (hatched region in Fig. 1*C*), with a larger amplitude for colder datasets (see *SI Appendix* for a temperature comparison). However, close to half-filling, we find the emergence of longer-range correlations marked by a nonzero tail in the sign-corrected correlations. Such a low-temperature feature was not observed in previous studies pertaining to the FHM on a square lattice (33, 39, 78). The core structure of the polarons are qualitatively well reproduced by dQMC and METTS simulations (solid and dashed lines in Fig. 4). While

the low-doping tail structure is not exhibited by METTS on the 32×4 cylinder, the geometric string model (dotted lines)—calculated using the coldest undoped dataset ($T/t \approx 0.29$, see *SI Appendix*)—shows a larger spatial extension despite a reduced core amplitude, and the dQMC is compatible with the onset of a tail. At larger doping, the geometric string calculations fail to reproduce the experimental data; we attribute this discrepancy to the relatively large contribution of doublon–hole fluctuations in our parameter regime ($U/t \approx 6.5$, see also *SI Appendix*). Note that the dQMC calculations around 12.5% are strongly affected by the sign problem (79), resulting in very large uncertainties.

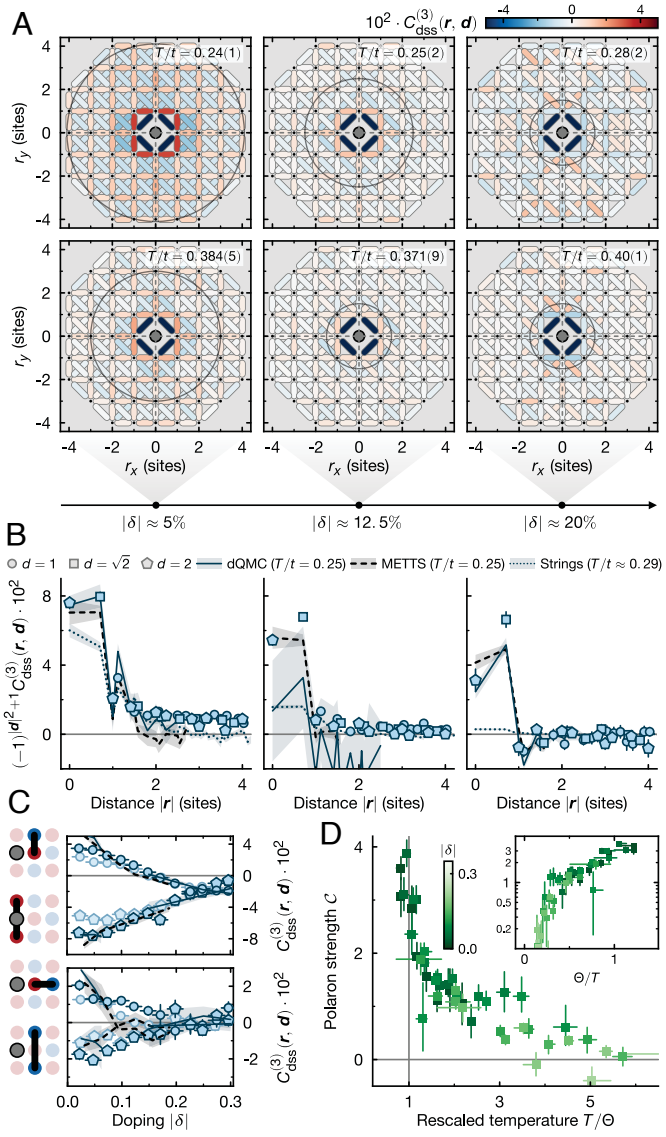

Fig. 4. Emergence of extended polarons in the pseudogap. (*A*) Example of polaron correlations $C_{\rm dss}(\boldsymbol{r}, \boldsymbol{d})$ at low temperature ($T/t \approx 0.25$, first row) and slightly larger temperature ($T/t \approx 0.4$, second row) and for different dopings. The maps are symmetrized, and the circle is a guide to the eye, indicating the distance over which correlations are sizeable. (*B*) Distance-averaged, sign-corrected polaron correlations associated to the coldest datasets (first row in *A*), for the same dopings. Different spin bonds ($|\boldsymbol{d}| = 1, \sqrt{2}, 2$ for NN, NNN (diagonal), and second NN bonds, respectively) are represented by different symbols. Solid, dashed, and dotted lines correspond to numerical simulations (dQMC, METTS, and geometric strings, respectively). (*C*) Polaronic correlations on selected bonds at short distances as a function of doping. Data points in dark (light) blue correspond to a temperature $T/t \approx 0.25$ ($T/t \approx 0.4$). (*D*) Strength of the polaron $\mathcal{C}$ (see text) as a function of the rescaled temperature T/Θ. The *Inset* depicts the same data in semi-log scale.

At larger dopings ($|\delta| \gtrsim 20\%$), the NN spin bond closest to the dopant changes sign. This feature, as well as a much-reduced temperature dependence, can be attributed to Fermi-Liquid behavior, in which the hole and spin correlations are dominated by the Pauli principle (78, 80). Such behavior sharply contrasts with the low doping behavior, where one sees the emergence of extended polarons at a temperature consistent with $T \lesssim \Theta$. These observations are illustrated in more detail in Fig. 4*C*, where $C^{(3)}_{\rm dss}(\boldsymbol{r}, \boldsymbol{d})$ is given as a function of doping for a few bonds closest to the dopant.

In analogy to the magnetic structure factor, which quantifies AFM strength, we propose to introduce a "polaron strength" $\mathcal{C}$ by integrating the sign-corrected correlations, $\mathcal{C} = \sum_{\boldsymbol{r},\boldsymbol{d}} (-1)^{|\boldsymbol{d}|^2+1} C_{\rm dss}(\boldsymbol{r}, \boldsymbol{d})$. In particular, we expect that the emergence of a long-range polaronic tail contributes significantly to $\mathcal{C}$. We show in Fig. 4*D* the polaron strength as a function of the rescaled temperature T/Θ. In the range of temperatures and dopings explored here (hatched region in Fig. 1*C*), we notice that the polaron strength follows a similar universal trend as found for the spin ordering. Specifically, it increases significantly when $T \leq \Theta$, signaling the importance of polaronic spin–charge correlations in the pseudogap regime. In the intermediate regime $1 \lesssim T/\Theta \lesssim 2$, $\mathcal{C}$ is dominated by the polaronic core, whose amplitude decreases as T/Θ increases. At large dopings ($T \gg \Theta$ in our datasets) the presence of sign-changed spin bonds cancels out the contribution from the polaronic core, such that $\mathcal{C}$ goes to zero.

4. Higher-Order Correlations

Quite generally, nonzero correlations beyond second-order constitute key signatures of strongly correlated regimes, as weakly correlated systems are well characterized by effective quasi-particle theories with Gaussian—and thus low-order—correlations. The third-order polaronic correlations explored above confirm the existence of a strongly correlated regime for $T \leq \Theta \simeq T^*$, associated with the pseudogap phase of the FHM. A natural extension consists in exploring higher-order correlations, which are accessible with our experimental apparatus.

We begin by considering the 4th-order normalized and connected spin correlations, defined as

$$C^{(4)}_{\mathcal{K}} = \frac{2^4}{\mathcal{N}_{\mathcal{K}}} \sum_{\substack{\boldsymbol{i} \in \Omega \\ \boldsymbol{i},\boldsymbol{j},\boldsymbol{k},\boldsymbol{\ell} \in \mathcal{K}}} \langle \hat{S}^z_{\boldsymbol{i}} \hat{S}^z_{\boldsymbol{j}} \hat{S}^z_{\boldsymbol{k}} \hat{S}^z_{\boldsymbol{\ell}} \rangle_c \,, \qquad [6]$$

where $\mathcal{K}$ designates a spatial arrangement of the four spins, and $\mathcal{N}_{\mathcal{K}}$ denotes the corresponding normalization factor. Here, we consider NN bonds or diagonal bonds only, i.e., spins arranged in a square ($C^{(4)}_{\square}$), or in a diamond-shape ($C^{(4)}_{\diamond}$) configuration (see *SI Appendix* for additional data corresponding to a T-shape configuration). The results are shown in Fig. 5*A* and *B*, where both the bare and the connected correlations are plotted against the rescaled temperature T/Θ. As expected from AFM order, the bare correlations are positive and increase in amplitude when the temperature is reduced. In the square configuration, the connected correlations become significantly nonzero and negative as $T \lesssim \Theta$, and corroborate the emergence of a strongly correlated regime with sizeable quantum fluctuations stemming from the underlying quantum antiferromagnet. In the case of the diamond-shaped configuration, which corresponds to more distant spins, connected correlations remain close to zero.

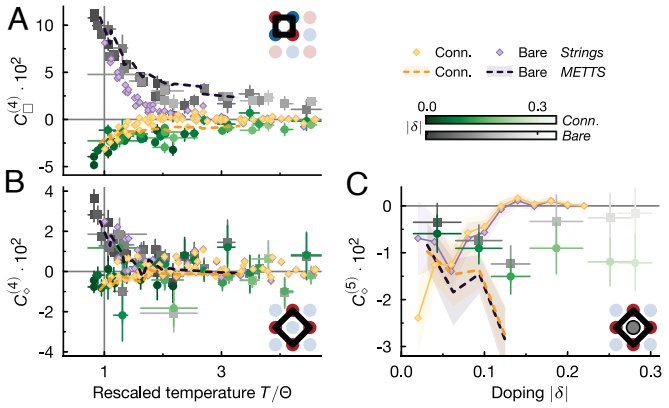

Fig. 5. Higher-order correlations. (*A* and *B*) 4th-order spin correlations with four spins arranged in a square (*A*), or in a diamond shape (*B*). The connected (bare) correlations, represented by green circles (gray squares), are plotted against the rescaled temperature T/Θ. The color scale indicates the doping. (*C*) 5th-order spin–charge correlations in the diamond configuration, showing that the presence of a dopant strongly affects the correlations. In all panels, the dashed lines and the dots correspond to METTS and geometric string calculations, respectively.

Overall, our results suggest that the role of quantum fluctuations, central in the emergence of strongly correlated states and nonzero high-order correlations, weakens as the distances between spins increase. In all cases, METTS (dashed lines) and geometric string (diamonds) calculations agree well with the experimental data.

Interestingly, we find significant qualitative and quantitative changes in the diamond-shape configuration when evaluated conditioned on the presence of a dopant at its center. More precisely, we evaluated the 5th-order normalized conditional dopant-spin correlations (81) (see *SI Appendix* for details),

$$C_{\mathcal{K}}^{(5)} = \frac{2^4}{\mathcal{N}_{\mathcal{K}}} \sum_{\substack{i\in\Omega \\ i,j,k,\ell,m\in\mathcal{K}}} \frac{\langle \hat{d}_i \hat{S}_j^z \hat{S}_k^z \hat{S}_\ell^z \hat{S}_m^z \rangle_c}{\langle \hat{d}_i \rangle} \Bigg|_{\text{cond. } \hat{d}_i} . \qquad [7]$$

To compensate for more limited statistics, the subsequent analysis employs broader doping intervals (10% rather than the 5% used previously). In Fig. 5*C*, $C_{\diamond}^{(5)}$ is plotted against doping for $T/t \approx 0.25$ (see *SI Appendix* for the T-shape configuration and for a comparison with higher temperatures). Close to half-filling, both the bare and conditioned correlations vanish due to dominant effects of doublon–hole fluctuations—each hole (doublon) is in the direct vicinity of a doublon (hole) and thereby voids the correlations. However, we measure significant nonzero values for $C_{\diamond}^{(5)}$ around $|\delta| = 10$ to 20% and, more importantly, the values are equal in amplitude to the bare correlations. This is in stark contrast to $C_{\diamond}^{(4)}$ (which is governed by the bare correlator) and suggests that the diamond-shape correlator is dominated by higher-order terms in the presence of a dopant.

Such a feature—dominant higher-order correlation—is characteristic of strongly correlated systems and can here be attributed to the presence of fluctuating chargon-spinon structures. It indicates that, upon entering the pseudogap, magnetic structures emerge that can only be revealed through higher-order correlations (and hence lie beyond our conventional understanding of Gaussian fluctuations). Our results furthermore suggest that these string-like correlations in the vicinity of dopants persist up to about 20% doping, providing an intuitive microscopic understanding of the nature of moving dopants and the formation of geometric strings (81). The METTS calculations (dashed lines), converged up to 12.5% doping, exhibit a trend consistent with the experimental data. The string-based calculation approach also captures the overall features of the experimental data, notably reproducing the dominance of higher-order correlations at finite doping. However, the string calculations show significant correlations only up to about 10% doping. This disagrees notably with METTS and with the experimental data, similarly to the dopant–spin–spin correlations (Fig. 4*B*). This discrepancy indicates that the geometric string framework—intrinsically linked to the physics of the weakly doped antiferromagnetic parent compound—does not quantitatively reproduce dopant-spin correlations within our parameter regime, although it remains accurate in capturing magnetic correlations (Fig. 5 *A* and *B*).

5. Discussion and Outlook

In this work, we have explored the FHM with a quantum gas microscope in a regime of temperature and doping in which numerical studies predict the existence of a pseudogap (Fig. 1*C*) (12, 19, 51). Our results, based on the evaluation of spin and dopant-spin correlations, reveal the emergence of a strongly correlated regime concomitant to the pseudogap. The peak spin structure factor, in particular, allows to extract a doping-dependent temperature scale Θ, which marks the transition to the strongly correlated regime. The temperature scale not only organizes the spin correlations into a universal scaling form but also matches the pseudogap temperature T^* extracted independently from the saturation of the magnetic susceptibility using METTS (Fig. 3). Recent unpublished numerical studies furthermore suggest that the energy scale Θ reproduces well the doping dependence of low-energy magnon excitations, thus providing an additional link to the underlying magnetic origin of the pseudogap (82). Taken together, these two findings imply that the pseudogap emerges concurrently with enhanced, albeit not infinitely extended, AFM correlations. Thus, Θ serves as a proxy for the underlying spin stiffness-like scale that sets the stage for pseudogap formation. Our work furthermore shows that this temperature scale governs the scaling behavior of higher-order spin and spin–charge correlations. In the temperature regime close to $T \sim \Theta$, we observe extended third-order polaronic dopant-spin correlations beyond the direct vicinity of the dopant (Fig. 4). Moreover, we have measured fifth-order dopant-spin correlations for which the contribution of lower-order terms is limited, suggesting that genuine quantum many-body correlations—beyond two or even three particles—dominate the system's physical properties upon entering the pseudogap. These higher-order correlators can additionally serve as benchmarks for testing the validity of different theoretical approaches.

Our work opens numerous perspectives for a better experimental understanding of the pseudogap phase in the FHM, with our main conclusions going in favor of a strong relation between spin correlations and the pseudogap. It was also suggested (83, 84) that the pseudogap phase, in analogy to the pseudogap in the context of the BEC-BCS crossover of strongly correlated Fermi gases, corresponds to the emergence of preformed pairs as a precursor to a superconducting state. Future studies beyond the scope of this work include the exploration of pairing among dopants, especially in the regime of extended polaronic tails (Fig. 4), where significant dopant-spin correlations

are measured at distances comparable to the mean distance between dopants $|\delta|^{-1/2}$. The emergence of hidden order has also been proposed as a characteristic of the pseudogap (22–24, 85), and could be explored using high-order correlation functions, which by nature reveal correlations beyond the two-point (Gaussian) level. At lower temperatures, one furthermore expects the emergence of a charge density wave (stripes), also associated with a shift of the peak in the spin structure factor away from (π, π). Such signatures were not observed in our experimental data and likely require reaching colder temperatures. This would also allow one to probe the possible connection of the pseudogap with the softening of the charge response associated with a maximum of the compressibility [Widom line (86)].

The momentum-space structure of the pseudogap is also an outstanding question for future studies. In the solid-state context, momentum-resolved measurements such as angular-resolved photoemission spectroscopy (ARPES) (71, 87) have revealed that the suppression of the density of states associated with the pseudogap occurs near the antinodal points of the Brillouin zone. Momentum-resolved measurements of the single-particle spectral function have so far remained out of reach of quantum gas microscope experiments, except in very specific configurations (see, e.g., ref. 88, in the case of the attractive Hubbard model). Nevertheless, ARPES techniques adapted to optical lattices (89) and quantum gas microscopy (90) have been proposed, offering a promising future direction. These approaches could enable the simultaneous acquisition of spectroscopic information and microscopic real-space correlation data, as presented here. Moreover, they would provide a platform to test theoretical predictions concerning the interplay between Fermi surface topology and the pseudogap (11).

Data, Materials, and Software Availability. The data supporting the findings of this study are available at Edmond (Open Research Data Repository of the Max Planck Society) and can be accessed via DOI: https://doi.org/10.17617/3.QRVUYR (91).

ACKNOWLEDGMENTS. We thank Thomas Schäfer, André-Marie Tremblay, Yury Vilk, and Eugene Demler for insightful discussions, as well as David Clément and Sarah Hirthe for careful reading of the manuscript. This work was supported by the Max Planck Society (MPG), the Horizon Europe program HORIZON-CL4-2022 QUANTUM-02-SGA (project 101113690, PASQuans2.1), the German Ministry of Education and Research (BMBF grant agreement 13N15890, FermiQP), and Germany's Excellence Strategy (EXC-2111-390814868). A.W. acknowledges support by the DFG through the Emmy Noether program (Grant No. 509755282). The Flatiron Institute is a division of the Simons Foundation. This research was supported in part by grant NSF PHY-2309135 to the Kavli Institute for Theoretical Physics (KITP). F.G. acknowledges support from the European Research Council (ERC) under the European Union's Horizon 2020 research and innovation programme (Grant Agreement No. 948141) - ERC Starting Grant SimUcQuam.

Author affiliations: [a]Max-Planck-Institut für Quantenoptik, Garching 85748, Germany; [b]Munich Center for Quantum Science and Technology, Munich 80799, Germany; [c]Institut d'Optique Graduate School, Laboratoire Charles Fabry, CNRS, Université Paris-Saclay, Palaiseau 91127, France; [d]Max Planck Institute for the Physics of Complex Systems, Dresden 01187, Germany; [e]Fakultät für Physik, Ludwig-Maximilians-Universität, Munich 80799, Germany; [f]Arnold Sommerfeld Center for Theoretical Physics, Ludwig-Maximilians-Universität, Munich 80333, Germany; [g]Lanzhou Center for Theoretical Physics, School of Physical Science and Technology, Key Laboratory of Quantum Theory and Applications of MoE, Key Laboratory of Theoretical Physics of Gansu Province, Lanzhou University, Lanzhou 730000, Gansu, China; [h]University of Regensburg, Regensburg 93053, Germany; [i]Collège de France, Paris Sciences et Lettres University, Paris 75005, France; [j]Center for Computational Quantum Physics, Flatiron Institute, New York, NY 10010; [k]École Polytechnique, Centre de Physique Théorique, CNRS, Paris F-91128, Palaiseau, France; [l]Department of Quantum Matter Physics, Université de Genève, Genève CH-1211, Suisse; and [m]Department of Physics, Scottish Universities Physics Alliance, University of Strathclyde, Glasgow G4 0NG, United Kingdom

1. J. Hubbard, B. H. Flowers, Electron correlations in narrow energy bands. *Proc. R. Soc. London, Ser. A, Math. Phys. Sci.* **276**, 238–257 (1963).
2. M. Qin, T. Schäfer, S. Andergassen, P. Corboz, E. Gull, The Hubbard model: A computational perspective. *Annu. Rev. Condens. Matter Phys.* **13**, 275–302 (2022).
3. M. Qin *et al.*, Absence of superconductivity in the pure two-dimensional Hubbard model. *Phys. Rev. X* **10**, 031016 (2020).
4. H. Xu *et al.*, Coexistence of superconductivity with partially filled stripes in the Hubbard model. *Science* **384**, eadh7691 (2024).
5. E. Morosan, D. Natelson, A. H. Nevidomskyy, Q. Si, Strongly correlated materials. *Adv. Mater.* **24**, 4896–4923 (2012).
6. P. A. Lee, N. Nagaosa, X. G. Wen, Doping a Mott insulator: Physics of high-temperature superconductivity. *Rev. Mod. Phys.* **78**, 17–85 (2006).
7. P. W. Anderson, The resonating valence bond state in La_2CuO_4 and superconductivity. *Science* **235**, 1196–1198 (1987).
8. E. Dagotto, Correlated electrons in high-temperature superconductors. *Rev. Mod. Phys.* **66**, 763–840 (1994).
9. A. M. S. Tremblay, B. Kyung, D. Sénéchal, Pseudogap and high-temperature superconductivity from weak to strong coupling. Towards a quantitative theory (Review Article). *Low Temp. Phys.* **32**, 424–451 (2006).
10. E. Gull, M. Ferrero, O. Parcollet, A. Georges, A. J. Millis, Momentum-space anisotropy and pseudogaps: A comparative cluster dynamical mean-field analysis of the doping-driven metal-insulator transition in the two-dimensional Hubbard model. *Phys. Rev. B* **82**, 155101 (2010).
11. W. Wu *et al.*, Pseudogap and fermi-surface topology in the two-dimensional Hubbard model. *Phys. Rev. X* **8**, 021048 (2018).
12. F. Šimkovic, R. Rossi, A. Georges, M. Ferrero, Origin and fate of the pseudogap in the doped Hubbard model. *Science* **385**, eade9194 (2024).
13. T. Timusk, B. Statt, The pseudogap in high-temperature superconductors: An experimental survey. *Rep. Prog. Phys.* **62**, 61 (1999).
14. M. R. Norman, D. Pines, C. Kallin, The pseudogap: Friend or foe of high T_C? *Adv. Phys.* **54**, 715–733 (2005).
15. H. Alloul, What is the simplest model that captures the basic experimental facts of the physics of underdoped cuprates? *C. R. Phys.* **15**, 519–524 (2014).
16. H. Alloul, T. Ohno, P. Mendels, ^{89}Y NMR evidence for a Fermi-liquid behavior in $YBa_2Cu_3O_{6+x}$ *Phys. Rev. Lett.* **63**, 1700–1703 (1989).
17. D. C. Johnston, Magnetic susceptibility scaling in $La_{2-x}Sr_xCuO_{4-y}$. *Phys. Rev. Lett.* **62**, 957–960 (1989).
18. O. Gunnarsson *et al.*, Fluctuation diagnostics of the electron self-energy: Origin of the pseudogap physics. *Phys. Rev. Lett.* **114**, 236402 (2015).
19. W. Wu, M. Ferrero, A. Georges, E. Kozik, Controlling Feynman diagrammatic expansions: Physical nature of the pseudogap in the two-dimensional Hubbard model. *Phys. Rev. B* **96**, 041105 (2017).
20. M. Frachet *et al.*, Hidden magnetism at the pseudogap critical point of a cuprate superconductor. *Nat. Phys.* **16**, 1064–1068 (2020).
21. S. A. Kivelson *et al.*, How to detect fluctuating stripes in the high-temperature superconductors. *Rev. Mod. Phys.* **75**, 1201–1241 (2003).
22. H. Schlömer, A. Bohrdt, F. Grusdt, Geometric orthogonal metals: Hidden antiferromagnetism and the pseudogap from fluctuating stripes. *PRX Quantum* **6**, 030342 (2025).
23. C. M. Varma, Pseudogap phase and the quantum-critical point in copper-oxide metals. *Phys. Rev. Lett.* **83**, 3538–3541 (1999).
24. B. Fauqué *et al.*, Magnetic order in the pseudogap phase of high-T_C superconductors. *Phys. Rev. Lett.* **96**, 197001 (2006).
25. K. M. Shen *et al.*, Nodal quasiparticles and antinodal charge ordering in $Ca_{2-x}Na_xCuO_2Cl_2$. *Science* **307**, 901–904 (2005).
26. M. Feld, B. Fröhlich, E. Vogt, M. Koschorreck, M. Köhl, Observation of a pairing pseudogap in a two-dimensional Fermi gas. *Nature* **480**, 75–78 (2011).
27. J. P. Gaebler *et al.*, Observation of pseudogap behaviour in a strongly interacting Fermi gas. *Nat. Phys.* **6**, 569–573 (2010).
28. X. Li *et al.*, Observation and quantification of the pseudogap in unitary Fermi gases. *Nature* **626**, 288–293 (2024).
29. M. Boll *et al.*, Spin- and density-resolved microscopy of antiferromagnetic correlations in Fermi-Hubbard chains. *Science* **353**, 1257–1260 (2016).
30. A. Mazurenko *et al.*, A cold-atom Fermi-Hubbard antiferromagnet. *Nature* **545**, 462–466 (2017).
31. M. Xu *et al.*, A neutral-atom Hubbard quantum simulator in the cryogenic regime. *Nature* **642**, 909–915 (2025).
32. C. S. Chiu *et al.*, String patterns in the doped Hubbard model. *Science* **365**, 251–256 (2019).
33. J. Koepsell *et al.*, Imaging magnetic polarons in the doped Fermi-Hubbard model. *Nature* **572**, 358–362 (2019).
34. G. Ji *et al.*, Coupling a mobile hole to an antiferromagnetic spin background: Transient dynamics of a magnetic polaron. *Phys. Rev. X* **11**, 021022 (2021).
35. M. L. Prichard *et al.*, Directly imaging spin polarons in a kinetically frustrated Hubbard system. *Nature* **629**, 323–328 (2024).
36. G. Salomon *et al.*, Direct observation of incommensurate magnetism in Hubbard chains. *Nature* **565**, 56–60 (2019).
37. M. Lebrat *et al.*, Observation of Nagaoka polarons in a Fermi-Hubbard quantum simulator. *Nature* **629**, 317–322 (2024).
38. M. Xu *et al.*, Frustration- and doping-induced magnetism in a Fermi-Hubbard simulator. *Nature* **620**, 971–976 (2023).
39. T. Hartke, B. Oreg, C. Turnbaugh, N. Jia, M. Zwierlein, Direct observation of nonlocal fermion pairing in an attractive Fermi-Hubbard gas. *Science* **381**, 82–86 (2023).
40. S. Hirthe *et al.*, Magnetically mediated hole pairing in fermionic ladders of ultracold atoms. *Nature* **613**, 463–467 (2023).

41. D. Bourgund *et al*., Formation of individual stripes in a mixed-dimensional cold-atom Fermi-Hubbard system. *Nature* **637**, 57–62 (2025).
42. P. T. Brown *et al*., Bad metallic transport in a cold atom Fermi-Hubbard system. *Science* **363**, 379–382 (2019).
43. M. A. Nichols *et al*., Spin transport in a Mott insulator of ultracold fermions. *Science* **363**, 383–387 (2019).
44. E. Guardado-Sanchez *et al*., Subdiffusion and heat transport in a tilted two-dimensional fermi-Hubbard system. *Phys. Rev. X* **10**, 011042 (2020).
45. J. LeBlanc *et al*., Solutions of the two-dimensional Hubbard model: Benchmarks and results from a wide range of numerical algorithms. *Phys. Rev. X* **5**, 041041 (2015).
46. T. Schäfer *et al*., Tracking the footprints of spin fluctuations: A MultiMethod, MultiMessenger study of the two-dimensional Hubbard model. *Phys. Rev. X* **11**, 011058 (2021).
47. B. X. Zheng *et al*., Stripe order in the underdoped region of the two-dimensional Hubbard model. *Science* **358**, 1155–1160 (2017).
48. E. W. Huang, C. B. Mendl, H. C. Jiang, B. Moritz, T. P. Devereaux, Stripe order from the perspective of the Hubbard model. *npj Quant. Mater.* **3**, 1–6 (2018).
49. P. Mai, S. Karakuzu, G. Balduzzi, S. Johnston, T. A. Maier, Intertwined spin, charge, and pair correlations in the two-dimensional Hubbard model in the thermodynamic limit. *Proc. Natl. Acad. Sci. U.S.A.* **119**, e2112806119 (2022).
50. B. Xiao, Y. Y. He, A. Georges, S. Zhang, Temperature dependence of spin and charge orders in the doped two-dimensional Hubbard model. *Phys. Rev. X* **13**, 011007 (2023).
51. A. Wietek, Y. Y. He, S. R. White, A. Georges, E. M. Stoudenmire, Stripes, antiferromagnetism, and the pseudogap in the doped Hubbard model at finite temperature. *Phys. Rev. X* **11**, 031007 (2021).
52. M. Meixner *et al*., Mott transition and pseudogap of the square-lattice Hubbard model: Results from center-focused cellular dynamical mean-field theory. *SciPost Phys.* **16**, 059 (2024).
53. A. Sinha, A. Wietek, Forestalled phase separation as the precursor to stripe order. *Nat. Commun*. **16**, 10807 (2025).
54. H. C. Jiang, T. P. Devereaux, Superconductivity in the doped Hubbard model and its interplay with next-nearest hopping t'. *Science* **365**, 1424–1428 (2019).
55. A. Wietek, Fragmented cooper pair condensation in striped superconductors. *Phys. Rev. Lett.* **129**, 177001 (2022).
56. N. Baldelli, H. Karlsson, B. Kloss, M. Fishman, A. Wietek, Fragmented superconductivity in the Hubbard model as solitons in Ginzburg–Landau theory. *npj Quant. Mater.* **10**, 1–9 (2025).
57. Y. F. Jiang, T. P. Devereaux, H. C. Jiang, Ground-state phase diagram and superconductivity of the doped Hubbard model on six-leg square cylinders. *Phys. Rev. B* **109**, 085121 (2024).
58. R. Blankenbecler, D. J. Scalapino, R. L. Sugar, Monte Carlo calculations of coupled boson-fermion systems. I.. *Phys. Rev. D* **24**, 2278–2286 (1981).
59. C. N. Varney *et al*., Quantum Monte Carlo study of the two-dimensional fermion Hubbard model. *Phys. Rev. B* **80**, 075116 (2009).
60. S. R. White, Minimally entangled typical quantum states at finite temperature. *Phys. Rev. Lett.* **102**, 190601 (2009).
61. E. M. Stoudenmire, S. R. White, Minimally entangled typical thermal state algorithms. *New J. Phys.* **12**, 055026 (2010).
62. A. Wietek *et al*., Mott insulating states with competing orders in the triangular lattice Hubbard model. *Phys. Rev. X* **11**, 041013 (2021).
63. F. Grusdt *et al*., Parton theory of magnetic polarons: Mesonic resonances and signatures in dynamics. *Phys. Rev. X* **8**, 011046 (2018).
64. I. Bloch, J. Dalibard, W. Zwerger, Many-body physics with ultracold gases. *Rev. Mod. Phys.* **80**, 885–964 (2008).
65. T. Esslinger, Fermi-Hubbard physics with atoms in an optical lattice. *Annu. Rev. Condens. Matter Phys.* **1**, 129–152 (2010).
66. T. Chalopin *et al*., Optical superlattice for engineering Hubbard couplings in quantum simulation. *Phys. Rev. Lett.* **134**, 053402 (2025).
67. N. D. Mermin, H. Wagner, Absence of ferromagnetism or antiferromagnetism in one- or two-dimensional isotropic Heisenberg models. *Phys. Rev. Lett.* **17**, 1133–1136 (1966).
68. F. Šimkovic IV, R. Rossi, M. Ferrero, Two-dimensional Hubbard model at finite temperature: Weak, strong, and long correlation regimes. *Phys. Rev. Res.* **4**, 043201 (2022).
69. D. P. Arovas, E. Berg, S. A. Kivelson, S. Raghu, The Hubbard model. *Annu. Rev. Condens. Matter Phys.* **13**, 239–274 (2022).
70. S. Chakravarty, B. I. Halperin, D. R. Nelson, Two-dimensional quantum Heisenberg antiferromagnet at low temperatures. *Phys. Rev. B* **39**, 2344–2371 (1989).
71. A. Damascelli, Z. Hussain, Z. X. Shen, Angle-resolved photoemission studies of the cuprate superconductors. *Rev. Mod. Phys.* **75**, 473–541 (2003).
72. X. Chen, J. P. F. LeBlanc, E. Gull, Simulation of the NMR response in the pseudogap regime of the cuprates. *Nat. Commun.* **8**, 14986 (2017).
73. M. S. Makivić, H. Q. Ding, Two-dimensional spin-1/2 Heisenberg antiferromagnet: A quantum Monte Carlo study. *Phys. Rev. B* **43**, 3562–3574 (1991).
74. Y. M. Vilk, A. M. S. Tremblay, Non-perturbative many-body approach to the Hubbard model and single-particle pseudogap. *J. Phys. I France* **7**, 1309–1368 (1997).
75. A. Abanov, A. V. Chubukov, J. Schmalian, Quantum-critical theory of the spin-fermion model and its application to cuprates: Normal state analysis. *Adv. Phys.* **52**, 119–218 (2003).
76. M. Ye, Z. Wang, R. M. Fernandes, A. V. Chubukov, Location and thermal evolution of the pseudogap due to spin fluctuations. *Phys. Rev. B* **108**, 115156 (2023).
77. J. M. Lihm, D. Kiese, S. S. B. Lee, F. B. Kugler, Enhanced electron-paramagnon scattering opens a pseudogap. The finite-difference parquet method (2025).
78. J. Koepsell *et al*., Microscopic evolution of doped Mott insulators from polaronic metal to Fermi liquid. *Science* **374**, 82–86 (2021).
79. S. Tarat, B. Xiao, R. Mondaini, R. T. Scalettar, Deconvolving the components of the sign problem. *Phys. Rev. B* **105**, 045107 (2022).
80. L. W. Cheuk *et al*., Observation of spatial charge and spin correlations in the 2d Fermi-Hubbard model. *Science* **353**, 1260–1264 (2016).
81. A. Bohrdt *et al*., Dominant fifth-order correlations in doped quantum antiferromagnets. *Phys. Rev. Lett.* **126**, 026401 (2021).
82. Private communication with E. Demler (2025).
83. V. J. Emery, S. A. Kivelson, Importance of phase fluctuations in superconductors with small superfluid density. *Nature* **374**, 434–437 (1995).
84. V. Mishra, U. Chatterjee, J. C. Campuzano, M. R. Norman, Effect of the pseudogap on the transition temperature in the cuprates and implications for its origin. *Nat. Phys* **10**, 357–360 (2014).
85. S. Chakravarty, R. B. Laughlin, D. K. Morr, C. Nayak, Hidden order in the cuprates. *Phys. Rev. B* **63**, 094503 (2001).
86. G. Sordi, P. Sémon, K. Haule, A. M. S. Tremblay, Pseudogap temperature as a Widom line in doped Mott insulators. *Sci Rep* **2**, 547 (2012).
87. J. A. Sobota, Y. He, Z. X. Shen, Angle-resolved photoemission studies of quantum materials. *Rev. Mod. Phys.* **93**, 025006 (2021).
88. P. T. Brown *et al*., Angle-resolved photoemission spectroscopy of a Fermi-Hubbard system. *Nat. Phys.* **16**, 26–31 (2020).
89. T. L. Dao, A. Georges, J. Dalibard, C. Salomon, I. Carusotto, Measuring the one-particle excitations of ultracold fermionic atoms by stimulated Raman spectroscopy. *Phys. Rev. Lett.* **98**, 240402 (2007).
90. A. Bohrdt, D. Greif, E. Demler, M. Knap, F. Grusdt, Angle-resolved photoemission spectroscopy with quantum gas microscopes. *Phys. Rev. B* **97**, 125117 (2018).
91. I. Bloch, Dataset for: Observation of emergent scaling of spin-charge correlations at the onset of the pseudogap. Edmond. https://doi.org/10.17617/3.QRVUYR. Deposited 5 January 2026.